PCCP

Accepted Manuscript

ROYAL SOCIETY OF CHEMISTRY

www.rsc.org/pccp

Physical Chemistry Chemical Physics
CREATED USING THE RSC LaTeX PCCP ARTICLE TEMPLATE – SEE www.rsc.org/electronicfiles FOR DETAILS
ARTICLE TYPE www. rsc.org/xxxxxx | XXXXXXXX

Local structure of semicrystalline P3HT films probed by nanofocused coherent x-rays†

Ruslan P. Kurta,[a,b*] Linda Grodd,[c] Eduard Mikayelyan,[c] Oleg Y. Gorobtsov,[a,d] Ivan A. Zaluzhnyy,[a,e] Ilaria Fratoddi,[f] Iole Venditti,[g] Maria Vittoria Russo,[g] Michael Sprung,[a] Ivan A. Vartanyants[a,e‡] and S. Grigorian[c§¶]

Received Xth XXXXXXXXXX 20XX, Accepted Xth XXXXXXXXX 20XX
First published on the web Xth XXXXXXXXXX 200X
DOI: 10.1039/b000000x

The hidden structural properties of semicrystalline polymer films are revealed by nanofocused x-ray scattering studies. X-ray cross-correlation analysis (XCCA) is employed to diffraction patterns from blends of poly(3-hexylthiophene) (P3HT) with gold nanoparticles (AuNPs). Spatially resolved maps of orientational distribution of crystalline domains allow us to distinguish sample regions of predominant face-on morphology, with a continuous transition to edge-on morphology. The average size of crystalline domains was determined to be of the order of 10 nm. As compared to pristine P3HT film, the P3HT/AuNPs blend is characterized by substantial ordering of crystalline domains, which can be induced by Au nanoparticles. The inhomogeneous structure of the polymer film is clearly visualized on the spatially resolved nanoscale 2D maps obtained using XCCA. Our results suggest that the observed changes of the polymer matrix within crystalline regions can be attributed to nanoconfinement in the presence of gold nanoparticles.

1 Introduction

Semicrystalline conjugated polymers are promising cost-effective candidates for organic electronic devices[1–3]. Polythiophenes, in particular poly(3-hexylthiophene) (P3HT) [see Fig. 1(c)], are among the most popular conjugated polymers used in organic electronics, in particular, for organic field-effect transistors (OFET) and solar cell applications[4–9]. Typical features of these polymers are mixtures of poor, disordered and well organized, crystalline domains[10,11]. Commonly, it is assumed that a higher degree of crystallinity substantially improves device efficiency[12–15]. Controlling the morphology and orientation of the crystalline domains in polymer films is a crucial step for the fabrication process, since it determines key electronic properties of the material, such as charge carrier mobility and charge separation, and defines the overall device performance[9,15,16].

The crystalline domain sizes of P3HT can be varied in the range of tens to few hundreds of nanometers, depending on preparation techniques[10,17,18]. In many cases two predominant morphologies, termed face-on and edge-on, can be observed for pristine P3HT[15,19]. They are defined by a different orientation of crystalline domains with respect to the substrate. P3HT lamellae stack parallel to the substrate in the case of face-on domains [Fig. 1(a)], and perpendicular in the case of edge-on domains [Fig. 1(b)]. The shortest distance between P3HT layers, called π-π stacking distance, is equal to $b/2$, where b is a unit cell parameter [Fig. 1(a),(b)]. Mixed orientation of domains also occurs, especially in non annealed samples. Generally, it is assumed that the face-on orientation is favorable for photovoltaic applications, while the edge-on orientation of domains enhances OFET performance[4,15,20].

P3HT films can be prepared using various methods, for example, drop-casting, spin-coating, dip-coating or directional crystallization, leading to a different degree of crystallinity and preferred orientation of P3HT domains[5,15,21,22]. The for-

† Electronic Supplementary Information (ESI) available. See DOI: 10.1039/b000000x/

[a] *Deutsches Elektronen-Synchrotron DESY, Notkestraße 85, D-22607 Hamburg, Germany.*
[b] *European XFEL GmbH, Albert-Einstein-Ring 19, D-22761 Hamburg, Germany.*
[c] *Department of Physics, University of Siegen, Walter-Flex-Straße 3, D-57072 Siegen, Germany.*
[d] *National Research Center "Kurchatov Institute", Kurchatov Square 1, 123182 Moscow, Russia.*
[e] *National Research Nuclear University MEPhI (Moscow Engineering Physics Institute), Kashirskoe shosse 31, 115409 Moscow, Russia.*
[f] *Department of Chemistry and Center for Nanotechnology for Engineering (CNIS), University of Rome Sapienza, P.le A. Moro 5, I-00185 Rome, Italy.*
[g] *Department of Chemistry, University of Rome Sapienza, P.le A. Moro 5, I-00185 Rome, Italy.*
[*] *E-mail: ruslan.kurta@xfel.eu*
[‡] *E-mail: ivan.vartaniants@desy.de*
[§] *E-mail: grigorian@physik.uni-siegen.de*
[¶] *Experiments were designed by S.G. and I.A.V. and performed by S.G., L.G., E.M., R.K., O.Y.G. and M.S.; samples were prepared by L.G., E.M., S.G. in collaboration with I.F., I.V. and M.V.R.; data analysis and interpretation was performed by R.K., I.A.Z. and I.A.V.; the manuscript was written by R.K. and I.A.V.; all authors discussed the results and commented on the manuscript.*

mation of a particular morphology of the film is defined by macromolecular parameters (molecular weight, regioregularity, polydispersity, etc), sample growth conditions (e.g., temperature, coating speed) and post-processing (e.g., annealing)[1,5,10,12,13,15,20–28]. It has been demonstrated that thermal annealing of the grown films results in better crystallinity and improved charge carrier mobility[13,14,20,25,29].

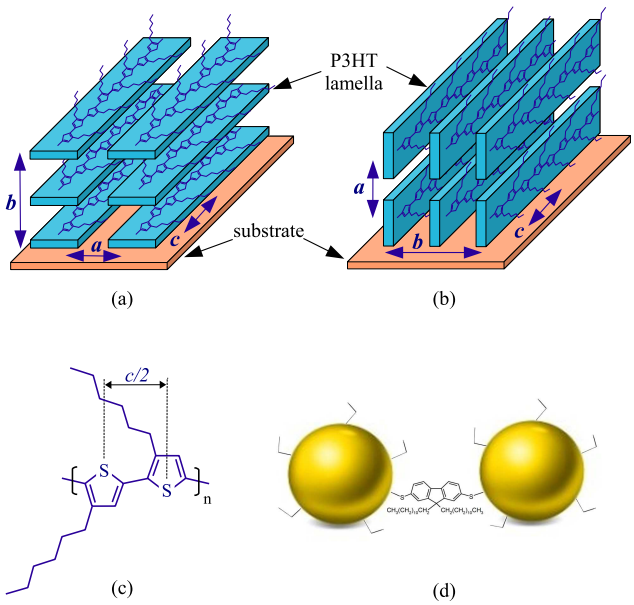

Fig. 1 Two types of predominant orientation of semicrystalline P3HT domains with respect to a substrate, the face-on (a) and edge-on (b) orientations. (c) Repeating unit of the P3HT polymer chain. (d) Gold nanoparticles stabilized with fluorene derivatives (AuNPs-SFL).

Together with pristine P3HT, its blends of various compositions emerge as another important class of hybrid materials with attractive structural and electronic properties[26,30,31]. In this work we analyzed structural variations of the P3HT host matrix upon small addition of gold nanoparticles stabilized with fluorene derivatives (AuNPs-SFL) [see Fig. 1(d)]. Such systems have been extensively investigated[32–34] and are considered to be attractive for optoelectronic applications due to their optical absorption and emission properties, as well as solubility[35–37].

It is important to characterize the structure of the π-π conjugated P3HT network on the nanoscale, since charge transport and charge separation are governed by the nanoscale morphology of a polymer film[3,23,38]. Various techniques, such as x-ray, electron or neutron scattering, atomic force microscopy and transmission electron microscopy, are used to experimentally characterize the sample morphology on different length scales[5,12,20,30]. To study structural variations in semicrystalline P3HT films on the nanoscale we performed spatially-resolved coherent x-ray scattering experiment with a nanofocused x-ray beam, in combination with the x-ray cross-correlation analysis (XCCA)[39–43]. A nanosize x-ray probe provides access to the local structure of a polymer film, and XCCA gives information on orientational ordering on a larger length scales. XCCA is a newly developed technique for structural characterization of partially ordered samples[44–47]. As it will be shown in our paper, this approach provides information which is complementary to results of conventional small angle x-ray scattering (SAXS) or grazing incidence x-ray diffraction (GIXD) experiments[25,26].

This paper is organized as follows. The description of the experimental setup, sample preparation and measurement scheme are presented in the second section of the paper. In the third section results of the data analysis are presented, where the average and spatially resolved structural properties of the film are considered separately. The conclusions section completes the paper.

2 Experimental

The x-ray experiment was performed at the GINIX endstation, P10 beamline, PETRA III[48]. The experimental details are described elsewhere[47]. The sample area of $20 \times 40\ \mu m^2$ was scanned with a nanobeam [$200 \times 300\ nm^2$ (FWHM), photon energy 13 keV] on the 20×40 raster grid with a $1\ \mu m$ step size in both directions and with the total number of $M = 800$ sample positions. Cryogenic cooling in combination with short exposure times of 0.3 sec per image were used to minimize radiation damage.

The sample was spin-cast from a blend of P3HT (molecular weight 44.9 kg/mol; PDI 1.22; regioregularity $> 98\%$) with gold nanoparticles. Gold nanoparticles of $2-3$ nm in size stabilized with fluorene derivatives (AuNPs-SFL) have been prepared and characterized in analogy to recent reports[32,49–52]. Briefly, AuNPs-SFL nanoparticles have been prepared starting from $HAuCl_4 \cdot 3H_2O$ in molar ratio 1 : 1 with the synthetic thiol 9,9-didodecyl-2,7-bis(acetylthio phenyl ethynyl) fluorene[32]. A solution of the fluorene dithiol (0.062 mmol for each sulphur functionality) in toluene (9 mL) was vigorously mixed with an aqueous solution containing the gold precursor (0.128 mmol, in 4 mL of deionized water) and tetraoctilammonium bromide (0.152 mmol) in 9 mL of toluene. After adding the reducing agent $NaBH_4$ (1.271 mmol) the mixture was allowed to react for 3 h at 25°C. The solid product AuNPs-SFL was recovered and purified; elemental analysis (%): C 39.97, H 5.18, S 5.50. UV-Vis ($CHCl_3$), λ_{max} (nm): 330, 530. X-ray photoelectron spectroscopy (XPS) and transmission electron microscopy (TEM) analysis reported in Ref.[32] supported the chemical structure of AuNPs-SFL herein reported. The solubility of AuNPs-SFL nanoparticles has been checked: the colloid suspension has a concentration limit of 2 mg/mL. The so-

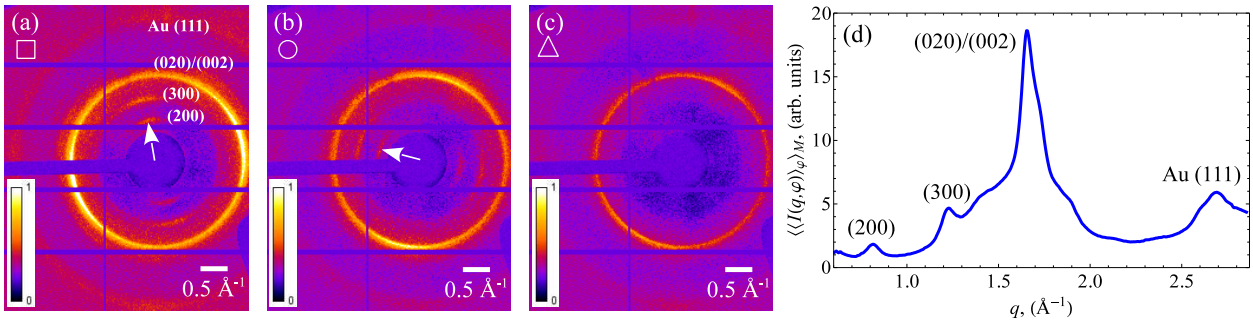

Fig. 2 (a),(b),(c) Diffraction patterns measured at three different positions of the polymer film, indicating the presence (a,b) and absence (c) of the face-on oriented P3HT domains. Diffraction patterns (a), (b) and (c) were measured at the sample positions indicated in Fig. 3(c) by a black square, circle and triangle, correspondingly. Arrows in (a) and (b) indicate orientation of the (200) peaks. (d) Ensemble averaged radial intensity profile $\langle\langle I(q,\varphi)\rangle_\varphi\rangle_M$.

lution was not filtered prior to spin coating, therefore a formation of aggregates cannot be completely excluded. A 5 mg/ml blend solution (P3HT:AuNPs-SFL = 10:1 by weight) in chloroform was spin cast on rectangular shaped grids with a 15 nm thick Si_3N_4 membranes (Dune Sciences, Inc.), with the spinning speed of 800 rpm. The drying process is rather fast for chloroform solution and typically films are dry after 60 seconds spinning. The time interval between sample fabrication and x-ray measurements was about few hours.

An x-ray dataset consisting of $M = 800$ diffraction patterns was measured. The data were corrected for background scattering and polarization of incident x-rays. Typical diffraction patterns corresponding to two different positions on the sample are shown in Figs. 2(a)-2(c). It is readily seen that the film is inhomogeneous, i.e. it has different structure at distinct sample positions.

3 Results and discussion

We first determine the average structure of the film and then continue with a spatially resolved analysis of nanoscale variations of the film properties. The detailed analysis of the average structural properties was presented in our previous paper[47]. Here we provide the main results of our analysis that will be necessary for complete understanding of the sample structure.

3.1 Spatially averaged structural properties

To determine the average structure of the film we first analyzed the ensemble-averaged intensity. The radial intensity $\langle\langle I(q,\varphi)\rangle_\varphi\rangle_M$ averaged over the full dataset M in the range of $0.6\ \text{Å}^{-1} \le q \le 2.9\ \text{Å}^{-1}$ is presented in Fig. 2(d). Our diffraction data suggest that the average structure of crystalline domains can be described with a monoclinic unit cell with parameters $a = 15.7$ Å and $b = c = 7.6$ Å, similar to the model proposed in[27]. One can clearly see in Fig. 2(d) the (200) and (300) peaks at $q = 0.82\ \text{Å}^{-1}$ and $q = 1.2\ \text{Å}^{-1}$, respectively *. These peaks are defined by the unit cell parameter a of crystalline P3HT domains [see Fig. 1], and suggest the presence of the face-on morphology in the sample. The strongest peak at $q = 1.65\ \text{Å}^{-1}$ may contain scattering contribution from both $c-$ and $b-$planes, since the c and b lattice parameters have very close values[25]. Due to the fact that crystalline domains may have different orientations in the illuminated sample area, this peak is often considered as $(020)/(002)$[16]. Finally, the peak located at $q = 2.68\ \text{Å}^{-1}$ is defined by scattering from the (111) set of atomic planes of gold. The corresponding scattering ring at higher momentum transfer values is partially visible on the diffraction patterns shown in Figs. 2(a)-2(c).

The average characteristics of orientational order in the film were determined in Ref.[47], where enhanced orientational order of P3HT domains was reported. We would like to note, that similar analysis of diffraction data measured from pristine P3HT films prepared by the same fabrication protocol did not reveal any orientational order in the system (see section 1.1 in the ESI†). This brings us to the conclusion that in P3HT/AuNPs blends orientational order of crystalline domains is induced by Au nanoparticles. This observation is supported by recent experiments, where improved crystallinity and orientational order were reported for various P3HT blends[31,53]. In the present case, a possible origin of orientational order is the effect of the pending $C_{12}H_{25}$ aliphatic groups on the fluorene spacer of AuNPs, that induces non covalent interaction with the P3HT polymer chains. This self assembly mechanism occurs in analogy to long-chain alkanethiols adsorbed onto gold surfaces.

The results of the ensemble-averaged XCCA[47] are defined by *average nanoscale* structural properties of the sample due to the nano-sized x-ray probe applied in the experiment. At

* The (100) reflection was covered by the beamstop.

the same time, the diffraction patterns shown in Figs. 2(a) and 2(b) clearly indicate structural variations in different parts of the sample. The major difference between these diffraction patterns is determined by the (200) and (300) peaks present in low q-region, that can be attributed to the face-on orientation of P3HT domains [Fig. 2(a),(b)]. Both peaks are absent in Fig. 2(c) where only the $(020)/(002)$ scattering ring can be observed, that is characteristic for the edge-on orientation. Therefore, it is important to characterize the structure of the polymer film at each separate position defined by the x-ray probe.

3.2 Spatially resolved structural properties

To determine spatially resolved nanoscale information about the structure of the film we analyzed diffraction patterns measured at different spatial positions of the sample. The measured intensity distribution $I(\mathbf{q})$ on a diffraction pattern can be considered in a polar coordinate system, where the momentum transfer vector $\mathbf{q} = (q, \varphi)$ is defined by the radial q and angular φ components. The scattered intensity $I(q, \varphi)$ can be expanded into angular Fourier series as

$$I(q,\varphi) = I_0(q) + 2\sum_{n=1}^{\infty} |I_n(q)| \cos(n\varphi + \psi_n), \qquad (1)$$

where $I_n(q)$ are, in general, complex Fourier components of intensity $I(q, \varphi)$ with the amplitudes $|I_n(q)|$ and phases ψ_n. To analyze local orientational distribution of domains we directly applied Eq. (1) and determined the phases ψ_2 of the dominant second order Fourier components $I_2(q)$. This Fourier component has the largest contribution in the spectrum and its phase determines local orientation of P3HT domains in the film[47].

We determined the distribution of orientations of crystalline P3HT domains across the sample using two-dimensional (2D) vector fields shown in Figs. 3(a) and 3(b). Each vector in these figures is defined by the amplitude and phase of the Fourier component $I_2(q)$, determined at the positions of the (200) [Fig. 3(a)] and $(020)/(002)$ [Fig. 3(b)] peaks, respectively. Figs. 3(d) and 3(e) represent all available orientations shown in Figs. 3(a) and 3(b) in the form of angular diagrams. The distribution of the magnitudes and orientations of the vectors in Figs. 3(a) and 3(b) shows that the film is not uniform. As it follows from Figs. 3(d) and 3(e), all phases are distributed in the angular range of $101^\circ \le \psi_2^{(200)} \le 164^\circ$ in Fig. 3(a), and in the range of $12^\circ \le \psi_2^{(020)/(002)} \le 90^\circ$ in Fig. 3(b). A comparison of vector orientations in Figs. 3(a) and 3(b) allows us to divide the sample area into two major regions [see Fig. 3(c)] according to the value of the phase difference $\Delta\psi_2 = \psi_2^{(200)} - \psi_2^{(020)/(002)}$ calculated at each spatial position.

The first region [red points in Fig. 3(c)] is characterized by a strong correlation between the vector orientations in Figs. 3(a) and 3(b), and the phase difference in the range of angles $80^\circ \le \Delta\psi_2 \le 90^\circ$. This suggests a presence of a certain preferential P3HT morphology in this region, that preserves angular orientation of the (200) and $(020)/(002)$ peaks with respect to each other at each particular position. Since our samples were prepared in the same way as in Ref.[20], where the face-on oriented domains were mainly observed, we conclude that the face-on morphology is preferential in this region. In this case, the main contribution to the peak at $q = 1.65$ Å^{-1} is defined by the c-planes [i.e., by the (002) peak]. As one can see in Fig. 3(c), two separated areas of the sample are characterized with dominating face-on morphology but different orientations, indicated with two arrows in Fig. 3(d). Quite naturally these regions coincide with the areas in Fig. 3(a) where the magnitudes $|I_2(q_{200})|$ are large since the face-on morphology in the given scattering geometry is primarily associated with a (200) peak.

The second region of the film [blue points in Fig. 3(c)] is characterized with a larger spread of the phase difference, $50^\circ \le \Delta\psi_2 \le 80^\circ$. One can see in Figs. 3(a) and 3(b), that both vector fields are characterized with a smooth change of the magnitudes and orientations of the vectors. At the same time, distribution of the magnitudes of the vectors in Fig. 3(b) is more uniform than in Fig. 3(a). It is about 50% of the vectors in Fig. 3(a) have magnitudes smaller than $1/3$ of the largest vector, while less than 5% of the vectors in Fig. 3(b) satisfy similar condition. This all suggests that in the second region a mixed orientation of domains is observed, and a continuous transition from the face-on towards the edge-on morphology is achieved by rotation of the face-on domains around the c-axis [see Fig. 1]. It is important to note, that such a conclusion can be drawn only from a simultaneous analysis of both vector fields [Fig. 3(a) and Fig. 3(b)] associated with two peaks, while separate analysis of each peak does not reflect a real distribution of domain types.

A smooth distribution of the phases and magnitudes of the Fourier components $I_2(q)$ across the sample shown in Figs. 3(a) and 3(b) indicates a substantial orientational order in the polymer film and suggests applicability of the spatially resolved XCCA to such a system. As a step further, we applied the cross-correlation function (CCF) $C(q, \Delta)$ to individual diffraction patterns to access hidden structural features of the film with an increased accuracy (see section 1.2 in the ESI†). Within this approach, the two-point CCF $C(q, \Delta)$ can be determined for each diffraction pattern as[40,41]

$$C(q,\Delta) = \langle I(q,\varphi) I(q,\varphi+\Delta) \rangle_\varphi , \qquad (2)$$

where Δ is the angular coordinate, and $I(q, \varphi)$ is the measured intensity. The CCF $C(q, \Delta)$ can be analyzed using a Fourier

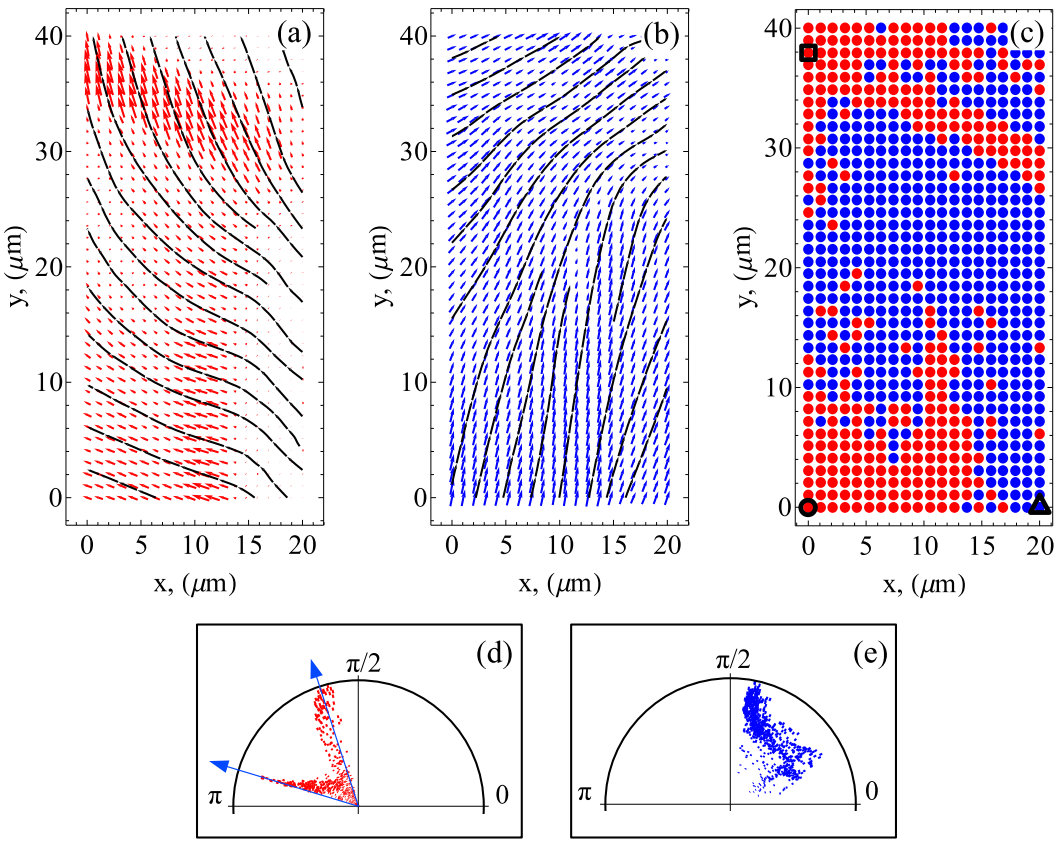

Fig. 3 Spatial distribution of orientations of crystalline P3HT domains across the film, determined by the phases $\psi_2^{(200)}$ and $\psi_2^{(020)/(002)}$ of the Fourier components $I_2(q_{200})$ (a) and $I_2(q_{020/002})$ (b), respectively. Each vector in the plotted vector fields corresponds to a certain position on the sample, with the vector length proportional to the modulus of the respective Fourier component. Black lines are plotted to guide the eye. (c) Two sample areas with predominant face-on (red points) and mixed (blue points) orientation of crystalline domains. A black square, circle and triangle in (c) indicate sample positions where diffraction patterns shown in Figs. 2(a-c) were measured. Angular distribution of all observed orientations in the vector fields (a) and (b) is shown in polar coordinates in (d) and (e), respectively. Arrows in (d) specify two major in-plane orientations of the face-on domains in the sample.

series decomposition similar to Eq. (1),

$$C(q,\Delta) = C_0(q) + 2\sum_{n=1}^{\infty} C_n(q)\cos(n\Delta), \qquad (3)$$

where $C_n(q)$ are the Fourier components of the CCF, which are directly related to the Fourier components of intensity $I_n(q)$ as[40–43], $C_n(q) = |I_n(q)|^2$ for $n \neq 0$, and $C_0(q) \equiv \langle I(q,\varphi)\rangle_\varphi^2$ for $n = 0$.

The Fourier components of intensity were determined using the relation $|I_n(q)| = \sqrt{C_n(q)}$. In Fig. 4 the magnitudes $|I_n(q)|$ of the Fourier components of the orders $n = 0$ and $n = 2$ are presented as a function of q for two diffraction patterns measured at different sample positions with the predominant face-on morphology. One can see that the q-dependence of $|I_2(q)|$ provides additional structural details that can not be directly observed in the angular averaged profile $|I_0(q)| \equiv \langle I(q,\varphi)\rangle_\varphi$, that is usually analyzed in scattering experiments. For example, the peak indexed as (102) on the $|I_2(q)|$ profile can be clearly separated from the (002) peak in Fig. 4(c), and is not visible in Fig. 4(d), indicating slightly different orientation of the face-on domains at these positions. This cannot be easily identified from the $|I_0(q)|$ profiles shown in Figs. 4(a) and 4(b).

We determined the positions of the centers q_0 and magnitudes $|I_n(q_0)|$ of different peaks in $|I_0(q)|$ and $|I_2(q)|$ profiles as a function of the probe position on the sample. These peaks were fitted with a Lorentzian function (see Fig. 4), $|I_n(q)| = b + s\cdot\gamma_n\cdot[(q-q_0)^2+\gamma_n^2]^{-1}$, where b is a background correction, s is a scaling coefficient, γ_n is half-width at half-maximum (HWHM) of the peak, and q_0 is a center of the peak. Analysis of the (200) peak on the $|I_0(q)|$ profile (see section

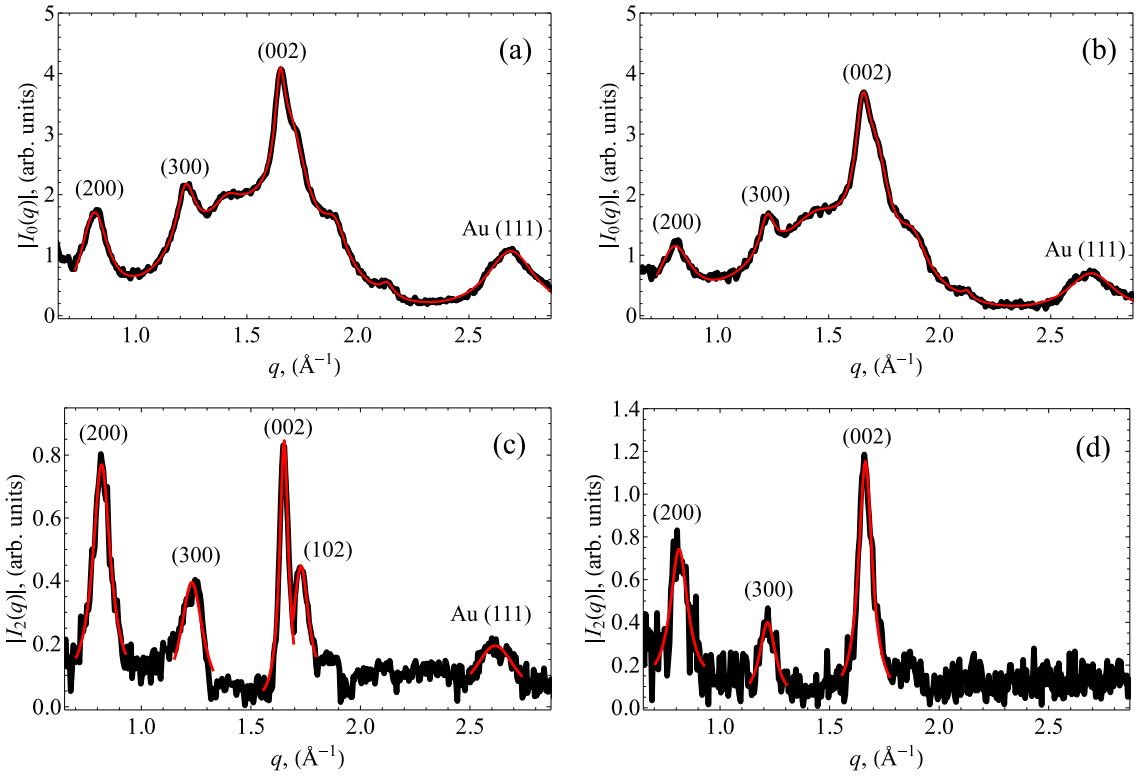

Fig. 4 Fourier components of intensity of the orders $n = 0$ (a),(b) and $n = 2$ (c),(d) as a function of q, calculated for two diffraction patterns measured at two sample positions with face-on morphology. Curves (a) and (c) correspond to the position indicated by a black square in Fig. 3(c), and (b) and (d) correspond to the position marked with a circle in Fig. 3(c). Black and red curves correspond to the experimental data and results of Lorentzian fits, respectively (see text). In the case of $n = 0$ a linear background contribution has been subtracted.

1.3 in the ESI†), gives the average positional correlation length $\xi = 2\pi/\gamma_0$ of the order of 10 nm. This value is in agreement with a characteristic size of P3HT crystalline domains[20,26].

In Fig. 5(a) a 2D map of the magnitudes $|I_0(q_0)|$ of the Au (111) peak is shown, determined from the fit of the (111) peak on the $|I_0(q)|$ profile. As one can see, gold nanoparticles are not uniformly distributed across the film, the regions with high gold concentration correspond to large values of Au (111) peak magnitude. A 2D map of the P3HT (002) peak center position q_0 determined from the $|I_2(q)|$ profile is shown in Fig. 5(b). One can clearly see a smooth variation of the (002) peak position, that indicates changes of the unit cell parameter c across the film in the range from 7.54 Å to 7.62 Å. In the regions with higher gold concentration the (002) peak slightly shifts to lower q. This observation suggests that Au nanoparticles could influence the structure of P3HT crystalline regions, particularly increase the c-spacing in the P3HT backbone [see Fig. 1].

4 Conclusions

The x-ray scattering experiment with a nanofocused beam in combination with XCCA allowed us to reveal details of the nanoscale structure of semicrystalline films cast from P3HT/AuNPs blend. We explored spatially resolved and average properties of the films by 2D mapping various structural parameters. One of the prominent results obtained in our work is orientational distribution of crystalline domains that allowed us to distinguish sample regions with predominant face-on and mixed orientation of domains. Our results suggest that a continuous transition between different morphologies is achieved by rotation of the domains around the c-axis defined along the P3HT backbone.

The polymer film is characterized by substantial orientational ordering of crystalline domains. As a result of our analysis we conclude that orientational order of P3HT domains can be induced by Au nanoparticles. Spatially resolved 2D maps show inhomogeneities in the spatial distribution of Au nanoparticles, where the regions with a high concentration of AuNPs coincide with regions where structural changes of

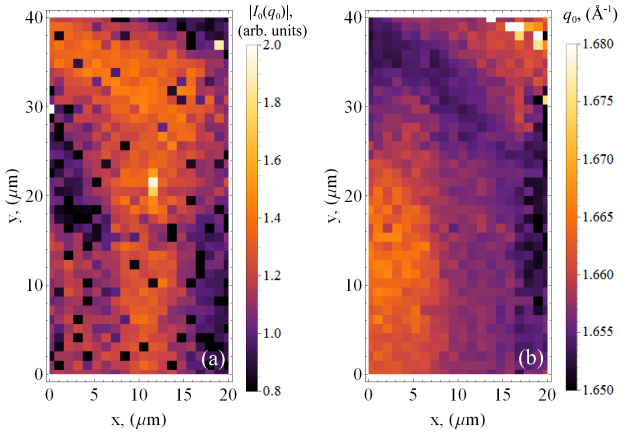

Fig. 5 Spatially resolved 2D maps of (a) magnitude $|I_0(q_0)|$ of Au (111) peak on the $|I_0(q)|$ profile, (b) position q_0 of the P3HT (002) peak determined on the $|I_2(q)|$ profile.

P3HT matrix are observed. The average size of crystalline domains was determined to be of the order of 10 nm.

The obtained results demonstrate that XCCA provides valuable information about the structure of partially ordered materials, complementary to the conventional SAXS or GIXD analysis. Spatially resolved analysis of the Fourier spectra of CCFs allows to observe structural features hidden in the averaged SAXS intensity, and to determine nanoscale variation and interplay between different film parameters. It is an irreplaceable tool to observe local structural changes in P3HT conjugated network induced by Au nanoparticles. As shown here, XCCA has a significant potential to be used as sensitive tool for nanoscale characterization of nanocomposite materials. The dependence of the polymer structure on the size/shape of nanoparticles and blend composition are among the relevant tasks that can be studied by means of XCCA.

5 Acknowledgements

We are grateful to S. Allard and U. Scherf from the University of Wuppertal, Germany for synthesis of the P3HT material. We are thankful to the group of T. Salditt, especially to M. Osterhoff and S. Kalbfleisch, for providing support of the Göttingen instrument for nano-imaging with x-rays (GINIX), and also A. Zozulya for the help during the experiment. We acknowledge fruitful discussions and support of this project by E. Weckert. We gratefully acknowledge U. Pietsch for helpful discussions. Part of this work was supported by BMBF Proposal 05K10CHG "Coherent Diffraction Imaging and Scattering of Ultrashort Coherent Pulses with Matter" in the framework of the German-Russian collaboration "Development and Use of Accelerator-Based Photon Sources" , the Virtual Institute VH-VI-403 of the Helmholtz Association, the Department of Chemistry of the Sapienza University of Rome through the Supporting Research Initiative 2013, the BMBF (project Nr 05K3PS4), and the Russian Science Foundation (grant 14-22-00098).

References

1 R. J. Kline, M. D. McGehee, E. N. Kadnikova, J. Liu, J. M. J. Fréche and M. F. Toney, *Macromolecules*, 2005, **38**, 3312.
2 L. A. Majewski, J. W. Kingsley, C. Balocco and A. M. Song, *Appl. Phys. Lett.*, 2006, **88**, 222108.
3 K. Coakley and M. McGehee, *Appl. Phys. Lett.*, 2004, **16**, 4533.
4 H. Sirringhaus, P. J. Brown, R. H. Friend, M. M. Nielsen, K. Bechgaard, B. M. W. Langeveld-Voss, A. J. H. Spiering, R. A. J. Janssen, E. W. Meijer, P. Herwig and D. M. de Leeuw, *Nature*, 1999, **401**, 685.
5 A. Salleo, R. J. Kline, D. M. Delongchamp and M. L. Chabinyc, *Adv. Mater.*, 2010, **22**, 3812.
6 M. T. Dang, L. Hirsch and G. Wantz, *Adv. Mater.*, 2011, **23**, 3597.
7 F. C. Krebs, N. Espinosa, M. Hösel, R. R. Sondergaard and M. Jorgensen, *Adv. Mater.*, 2013, **26**, 29.
8 Y. Y. Kim, S. Cook, S. M. Tuladhar, S. A. Choulis, J. N. J. R. Durrant, D. D. C. Bradley, M. Giles, I. McCulloch, C.-S. Ha and M. A. Ree, *Macromolecules*, 2006, **39**, 5843.
9 G. Nagarjuna and D. Venkataraman, *J. Polym. Sci.*, 2012, **50**, 1045.
10 P. Kohn, S. Hüttner, H. Komber, V. Senkovskyy, R. Tkachov, A. Kiriy, R. H. Friend, U. Steiner, W. T. S. Huck, J.-U. Sommer and M. Sommer, *J. Am. Chem. Soc.*, 2012, **134**, 4790.
11 M. Brinkmann and P. Rannou, *Adv. Funct. Mater.*, 2007, **17**, 101.
12 R. J. Kline, M. D. McGehee, E. N. Kadnikova, J. Liu and J. M. J. Fréchet, *Adv. Mater.*, 2003, **15**, 1519.
13 A. A. Zen, J. Pflaum, S. Hirschmann, W. Zhuang, F. Jaiser, U. Asawapirom, J. P. Rabe, U. Scherf and D. Neher, *Adv. Funct. Mater.*, 2004, **14**, 757.
14 K. Ali, U. Pietsch and S. Grigorian, *J. Appl. Cryst.*, 2013, **46**, 908.
15 N. Tanigaki, Y. Ikeo, T. Mizokuro, C. Heck and H. Aota, *Jap. J. Appl. Phys.*, 2014, **53**, 01AB05.
16 S. Joshi, S. Grigorian, U. Pietsch, P. Pingel, A. Zen, D. Neher and U. Scherf, *Macromolecules*, 2008, **41**, 6800.
17 T. J. Prosa, M. J. Winokur, J. Moulton, P. Smith and A. J. Heeger, *Macromolecules*, 1992, **25**, 4364.
18 K. Rahimi, I. Botiz, N. Stingelin, N. Kayunkid, M. Sommer, F. P. Koch, H. Nguyen, O. Coulembier, P. Dubois, M. Brinkmann and G. Reiter, *Angew. Chem. Int. Ed. Engl.*, 2012, **51**, 11131.
19 D. H. Kim, Y. Jang, Y. D. Park and K. Cho, *Macromolecules*, 2006, **39**, 5843.
20 T. S. Salammal, E. Mikayelyan, S. Grigorian, U. Pietsch, N. Koenen, U. Scherf, N. Kayunkid and M. Brinkmann, *Macromolecules*, 2012, **45**, 5575.
21 T. S. Shabi, S. Grigorian, M. Brinkmann, U. Pietsch, N. Koenen, N. Kayunkid and U. Scherf, *J. Appl. Polym. Sci.*, 2012, 2335.
22 M. Brinkmann and J. C. Wittmann, *Adv. Mater.*, 2006, **18**, 860.
23 H. Hoppe and N. Sariciftci, *J. Mater. Res.*, 2004, **19**, 1924.
24 R. Zhang, B. Li, C. M. Iovu, M. Jeffries-EL, G. Sauve, J. Cooper, S. Jia, S. Tristram-Nagle, D. M. Smilgies, D. N. Lambeth, R. D. McCullough and T. Kowalewski, *J. Am. Chem. Soc.*, 2006, **128**, 3480.
25 S. Grigorian, S. Joshi and U. Pietsch, *IOP Conf. Series: Mat. Sci. and Engineering*, 2010, **14**, 012007.
26 P. Kohn, Z. Rong, K. H. Scherer, A. Sepe, M. Sommer, P. Müller-

Buschbaum, R. H. Friend, U. Steiner and S. Hüttner, *Macromolecules*, 2013, **46**, 4002.
27 N. Kayunkid, S. Uttiya and M. Brinkmann, *Macromolecules*, 2010, **43**, 4961.
28 G. M. Newbloom, K. M. Weigandt and D. C. Pozzo, *Macromolecules*, 2012, **45**, 3452.
29 S. Joshi, P. Pindel, S. Grigorian, T. Panzner, U. Pietsch, D. Neher, M. Forster and U. Scherf, *Macromolecules*, 2009, **42**, 4651.
30 R. S. Moghaddam, S. Huettner, Y. Vaynzof, C. Ducati, G. Divitini, R. H. Lohwasser, K. P. Musselman, A. Sepe, M. R. J. Scherer, M. Thelakkat, U. Steiner and R. H. Friend, *Nano Lett.*, 2013, **13**, 4499.
31 O. Parashchuk, S. Grigorian, E. Levin, V. Bruevich, K. Bukunova, I. Golovnin, T. Dittrich, K. Dembo, V. Volkov and D. Paraschuk, *J. Phys. Chem. Lett*, 2013, **4**, 1298.
32 M. Quintiliani, M. Bassetti, C. Pasquini, C. Battocchio, M. Rossi, F. Mura, R. Matassa, L. Fontana, M. V. Russo and I. Fratoddi, *J. Mater. Chem. C*, 2014, **2**, 2517.
33 C. Battocchio, F. Porcaro, S. Mukherjee, E. Magnano, S. Nappini, I. Fratoddi, M. Quintiliani, M. V. Russo and G. Polzonetti, *J. Phys. Chem. C*, 2014, **118**, 8159.
34 C. Battocchio, I. Fratoddi, L. Fontana, E. Bodo, F. Porcaro, C. Meneghini, I. Pis, S. Nappini, S. Mobilio, M. V. Russo and G. Polzonetti, *Phys. Chem. Chem. Phys.*, 2014, **16**, 11719.
35 I. Venditti, I. Fratoddi, M. V. Russo and A. Bearzotti, *Nanotechnology*, 2013, **24**, 155503.
36 C. Battocchio, C. Meneghini, I. Fratoddi, I. Venditti, M. V. Russo, G. Aquilanti, C. Maurizio, F. Bondino, R. Matassa, M. Rossi, S. Mobilio and G. Polzonetti, *J. Phys. Chem. C*, 2012, **116**, 19571.
37 S. K. Ghosh and T. Pal, *Chem. Rev.*, 2007, **107**, 4797.
38 T. M. Clarke and J. R. Durrant, *Chem. Rev.*, 2010, **110**, 6736.
39 P. Wochner, C. Gutt, T. Autenrieth, T. Demmer, V. Bugaev, A. Diaz-Ortiz, A. Duri, F. Zontone, G. Grübel and H. Dosch, *Proc. Nat. Acad. Sci.*, 2009, **106**, 11511.
40 M. Altarelli, R. P. Kurta and I. A. Vartanyants, *Phys. Rev. B*, 2010, **82**, 104207; Erratum: 2012, 86, 179904(E).
41 R. P. Kurta, M. Altarelli, E. Weckert and I. A. Vartanyants, *Phys. Rev. B*, 2012, **85**, 184204.
42 R. P. Kurta, R. Dronyak, M. Altarelli, E. Weckert and I. A. Vartanyants, *New J. Phys.*, 2013, **15**, 013059.
43 R. P. Kurta, M. Altarelli and I. A. Vartanyants, *Adv. Cond. Matt. Phys.*, 2013, **2013**, 959835.
44 R. P. Kurta, B. I. Ostrovskii, A. Singer, O. Y. Gorobtsov, A. Shabalin, D. Dzhigaev, O. M. Yefanov, A. V. Zozulya, M. Sprung and I. A. Vartanyants, *Phys. Rev. E*, 2013, **88**, 044501.
45 M. A. Schroer, C. Gutt and G. Grübel, *Phys. Rev. E*, 2014, **90**, 012309.
46 A. C. Y. Liu, M. J. Neish, G. Stokol, G. A. Buckley, L. A. Smillie, M. D. de Jonge, R. T. Ott, M. J. Kramer and L. Bourgeois, *Phys. Rev. Lett.*, 2013, **110**, 205505.
47 R. P. Kurta, L. Grodd, E. Mikayelyan, O. Y. Gorobtsov, I. Fratoddi, I. Venditti, M. Sprung, S. Grigorian and I. A. Vartanyants, *J.Phys: Conf.Series*, 2014, **499**, 012021.
48 S. Kalbfleisch, H. Neubauer, S. P. Kruger, M. Bartels, M. Osterhoff, D. D. Mai, K. Giewekemeyer, B. Hartmann, M. Sprung and T. Salditt, *AIP Conf. Proc.*, 2011, **1365**, 96.
49 I. Fratoddi, I. Venditti, C. Battocchio, G. Polzonetti, F. Bondino, M. Malvestuto, E. Piscopiello, L. Tapfer and M. V. Russo, *J. Phys. Chem. C*, 2011, **115**, 15198.
50 R. Matassa, I. Fratoddi, M. Rossi, C. Battocchio, R. Caminiti and M. V. Russo, *J. Phys. Chem. C*, 2012, **116**, 15795.
51 R. Vitaliano, I. Fratoddi, I. Venditti, G. Roviello, C. Battocchio, G. Polzonetti and M. V. Russo, *J. Phys. Chem. A*, 2009, **113**, 14730.
52 C. Cametti, I. Fratoddi, I. Venditti and M. V. Russo, *Langmuir*, 2011, **27**, 7084.
53 W.-R. Wu, U.-S. Jeng, C.-J. Su, K.-H. Wei, M.-S. Su, M.-Y. Chiu, C.-Y. Chen, W.-B. Su, C.-H. Su and A.-C. Su, *ASC Nano*, 2011, **5**, 6233.